Palaeogeography, Palaeoclimatology, Palaeoecology 675 (2025) 113094

Contents lists available at ScienceDirect

Palaeogeography, Palaeoclimatology, Palaeoecology

journal homepage: www.elsevier.com/locate/palaeo

Holocene hydroclimate inferred from alkane isotope and pollen records from monsoonal northern Australia

Michael I. Bird [a,*], Michael Brand [b], Rainy Comley [b], Xennephone Hadeen [b], Niels C. Munksgaard [b], Cassandra Rowe [a], Christopher M. Wurster [b,1], Costijn Zwart [b]

[a] ARC Centre of Excellence for Indigenous and Environmental Histories and Futures, College of Science and Engineering, James Cook University, Cairns, QLD 4870, Australia
[b] ARC Centre of Excellence of Australian Biodiversity and Heritage, College of Science and Engineering, James Cook University, Cairns, QLD 4870, Australia

ARTICLE INFO

Editor: Amy Prendergast

Keywords:
Monsoon
Savanna
Biomarker
ENSO
Lacustrine
Palaeoclimate
Holocene

ABSTRACT

Terrestrial proxy records of environmental change from the southern end of the coupled East Asian-IndoAustralian monsoon domain remain limited in number. Here we present multi-proxy Holocene *n*-alkane hydrogen isotope and pollen records from Girraween Lagoon, located in monsoonal northern Australia. We compare the Girraween record with two published speleothem isotope records available to the north and south of the lagoon, all within the region where rainfall is dominantly associated with the southward movement of the Intertropical Convergence Zone (ITCZ) in the Austral summer. All three sites record an initial period of general monsoon intensification between ~7.5 and 9 ka, but after this time the responses of the three records diverge. The records from the northern and southern sites reflect changes in the mean position of the ITCZ at its periphery that did not impact the Girraween site. The Girraween record clearly demonstrates a period of particularly enhanced monsoon rainfall between 3 and 5 ka. This period, when rainfall was dominated by deep convection was initiated by a sustained southerly shift in mean ITCZ position, which also resulted in a reduction in rainfall in southern Indonesia. Weakening of the monsoon at the Girraween site was initiated by strengthened ENSO teleconnections at 2.5–3 ka and was accompanied movement of the ITCZ to a more northerly position resulting in enhanced rainfall in southern Indonesia. The monsoon regime that was fully established by ~2 ka at Girraween Lagoon, has broadly been in place since that time.

1. Introduction

Climate over much of the seasonal tropics is dominated by the monsoons, defined by a seasonal reversal of surface winds and associated large differences in rainfall amounts between the summer (wet) and winter (dry) season (Wang et al., 2017). The Indonesian-Australian summer monsoon (IASM) represents an extensive southern hemisphere monsoon system. It is anchored in the south by the Australian continent, coupled through the 'maritime continent' (Indonesia and insular Malaysia) and Indo-Pacific Warm Pool (IPWP) to the Northern Hemisphere East Asian Summer Monsoon (EASM) (Wyrwoll et al., 2007; Wang et al., 2017). The regions at the southern end of the IASM currently experience strong seasonality in rainfall with a well-defined wet season from December to March associated with the inflow of moist air from the northwest and a prolonged dry season from April to November dominated by trade winds from the southeast (Cook and Heerdegen, 2001).

There are three dominant air mass trajectories that deliver rainfall during the monsoon season in northern Australia. The first is the maritime continent to the northeast linked to cross-equatorial airflow and the EASM. The second is derived from the mid-latitudes of the southern hemisphere, arriving in northern Australia from the west after clockwise passage across the Indian Ocean, mediated by the Pilbara heat low. The third is derived from air masses arriving from the east, bearing moisture sourced from the Coral Sea and Gulf of Carpentaria (Pope et al., 2009). Suppiah (1992) categorised central northern Australia as the 'true' monsoon domain dominated by rain-bearing air masses arriving from the maritime continent, and western northern Australia as the 'pseudo-monsoon' domain characterised by air masses making landfall from the western Indian Ocean (Fig. 1). In reality, there is no firm boundary

* Corresponding author.
E-mail address: michael.bird@jcu.edu.au (M.I. Bird).
[1] Current address: Isotrace NZ Ltd., 167 High St, Dunedin, New Zealand.

https://doi.org/10.1016/j.palaeo.2025.113094
Received 13 March 2025; Received in revised form 9 June 2025; Accepted 10 June 2025
Available online 16 June 2025

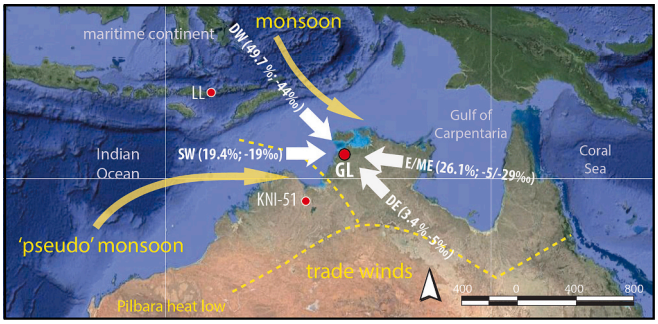

Fig. 1. Location of Girraween lagoon (GL), KNI-51 and Liang Luar (LL) along with other locations mentioned in the text. The general monsoon domain classification scheme of Suppiah (1992) shown in yellow. The generalised wind directions associated with the rainfall regimes identified by Pope et al. (2009) are shown as white arrows for Deep West (DW), Shallow West (SW), East (E), Moist East (ME) and Dry East (DE). Also shown is the percentage of total rainfall associated with each of these regimes and the amount-weighted hydrogen isotope composition of the rainfall from 2014 to 2018 (Zwart et al., 2018). Note that E and ME are similar in direction, and have been combined for clarity of the figure. (For interpretation of the references to colour in this figure legend, the reader is referred to the web version of this article.)

between these two domains, and moisture sourced from the Indian Ocean can deliver rainfall across western and northern Australia, with westerly wind bursts thought to trigger active monsoon phases (Hung and Yanai, 2004). It is likely that the balance between these two sources of moisture has changed in the past in response to changing orbital parameters (Wyrwoll et al., 2012).

Rainfall variability is tightly coupled to the occurrence of monsoon 'burst' and 'break' periods, modulated by wider atmospheric phenomena that vary on a range of timescales (Wheeler and McBride, 2005). The Madden-Julian Oscillation (MJO) and cyclogenesis impact rainfall amount on intra-annual timescales while the El Niño-Southern Oscillation (ENSO) and Indian Ocean Dipole (IOD) currently exert significant control over total rainfall amount on inter-annual timescales (Charles et al., 2016; Heidemann et al., 2023). In addition to annual rainfall amount, the distribution of rainfall in the pre- and post- monsoon seasons in northern Australia also exhibits significant ENSO-related variability. Up to 30 % of annual rainfall can fall in the transitional period before monsoon onset (Pope et al., 2009), and this is critical to the timing of ecological processes such as leaf flush/fall and grass growth in the wet-dry tropical savannas of northern Australia (Cook and Heerdegen, 2001).

In northern Australia, as in other parts of the world influenced by strongly monsoonal climates (Caley et al., 2011; Wang et al., 2017), rainfall variability associated with interactions between monsoon circulation and other atmospheric phenomena, including ENSO and cyclogenesis, leads to episodic drought and flood events (D'Arrigo et al., 2008; Kiem et al., 2016). These represent a key risk to agriculture, infrastructure and, more broadly, to sustainable ecosystem function across northern Australia (Dey et al., 2019). As climate changes in the future in response to anthropogenic forcing, it is also likely that rainfall variability and the incidence of extreme events will also change across the region, although the direction and magnitude of change are less well known than the trends in future temperature (Dey et al., 2019). In northern Australia, this is because it is not clear how the phase, amplitude and intensity of ENSO will interact with the monsoon and other sources of climate variability in the future (Charles et al., 2016), although modelling suggests that ENSO linkages will be strengthened as climate warms in the future (Xu et al., 2023).

Climate has varied substantially in the past and this variability is archived in a variety of palaeoenvironmental proxy records (Wang et al., 2017). In tropical monsoon regions, these records potentially provide insight into the range of hydroclimate variability in the past and into the interactions between the range of processes driving monsoon hydroclimate (Caley et al., 2011; Wang et al., 2017). In monsoon regions globally, the major sources of proxy hydroclimate information are the oxygen isotope ($\delta^{18}O$) composition of speleothem carbonate (Lachniet, 2009) and the hydrogen isotope ($\delta^{2}H$) composition of *n*-alkanes preserved in sedimentary archives (e.g. Garcin et al., 2012)

On glacial-interglacial timescales in the IASM-EASM region, speleothem isotope records have demonstrated that Milankovitch forcing drives changes in monsoon hydroclimate (Wang et al., 2017), ultimately through changing solar insolation, as well as through control of sea level and thereby the area of ocean available for evaporation across the maritime continent (Griffiths et al., 2009). Insolation changes on orbital timescales lead to changes in monsoon strength manifest in latitudinal shifts in the position of the Inter-tropical Convergence Zone (ITCZ), and therefore the position of highest seasonal rainfall in the IASM region (e.g. Griffiths et al., 2009).

While there are multiple speleothem isotope records of monsoon hydroclimate variability through the Holocene available for the EASM (e.g. Chen et al., 2016) and equatorial maritime continent regions (e.g. Wurtzel et al., 2018), there are comparatively few records available from northern Australia. Speleothem records that span the Holocene are limited to those that comprise the composite KNI-51 record from a cave near Kununurra in Western Australia (Denniston et al., 2013a), with some data available from the late Holocene from eastern tropical Australia (Haig et al., 2014) and the early to mid- Holocene from Ball Gown Cave (Denniston et al., 2017) and Cape Range (Denniston et al., 2013b) records, both also in Western Australia. To the north, in Southern Indonesia, there is a Holocene speleothem record from Liang Luar on the island of Flores (Ayliffe et al., 2013; Scroxton et al., 2022). During the Holocene, these speleothem isotope records have demonstrated substantial decadal to millennial scale variability in monsoon hydroclimate related to dynamic interactions between the IASM and EASM modulated by other coupled atmosphere-ocean phenomena.

Other information on Holocene hydroclimate in the region, generally of lower temporal resolution, has been derived from palynological (e.g. Shulmeister and Lees, 1995; McGowan et al., 2012; Field et al., 2017) and geomorphic (Wyrwoll and Miller, 2001; Wasson et al., 2007; May et al., 2015) records onshore as well as inferred from geochemical measures thought to reflect changing runoff intensity derived from marine sediment records from offshore Western Australia (Ishiwa et al., 2019), the Timor Sea (Kuhnt et al., 2015), south of Java (Mohtadi et al., 2011) and between Flores and Sumba (Steinke et al., 2014a, 2014b). Collectively, these records of Holocene hydroclimate change in the southern AISM region show both similarities and differences in trends, timing and magnitude of changes, and in the interpretation of the mechanisms driving inferred hydroclimatic change through the Holocene.

The hydrogen isotope composition of plant waxes (long chain alkanes and fatty acids) have shown considerable potential for reconstruction of changes in tropical hydroclimate (e.g. Vogts et al., 2016). Despite this potential, there are few *n*-alkane hydrogen-isotope records from the IASM region. A long chain *n*-alkane and fatty acid hydrogen isotope records for the IASM region has been developed from the sediments in Lakes on Sulawesi in Indonesia (Konecky et al., 2016; Parish et al., 2024), and a marine *n*-alkane hydrogen isotope record from the Indian Ocean off Java (Ruan et al., 2019). There are no records from northern Australia. Here we present the first *n*-alkane hydrogen isotope record spanning the Holocene derived from sediments preserved in Girraween lagoon, near Darwin in northern Australia. We compare our results with the aquatic pollen record from Girraween Lagoon (Rowe et al., 2019) to derive a record of hydroclimate change at the sire and compare this record with other published proxies of Holocene hydroclimate change from the southern IASM region.

2. Study area and Methods

This study builds on previously published work at Girraween Lagoon (Rowe et al., 2019; Bird et al., 2024; Hadeen et al., 2025), with more details on the site available in those studies. Here, we add a modern times series of water isotope composition in rainfall and in the lake waters, and a high-resolution *n*-alkane hydrogen isotope data covering the last 9000 years. We focus on this period because cognate terrestrial datasets from the broader region are available (Denniston et al., 2013a; Scroxton et al., 2022), and because interpretation is not complicated by impacts on rainfall amount and isotope composition that are linked to large changes (>300 km) in coastline position that occurred during deglaciation (Du et al., 2021; Bird et al., 2024). Sun et al. (2025) has demonstrated from BrGDGT analysis of the Girraween record that temperature at the site has warmed by ~2 °C over the course of the Holocene.

The pollen methods and data are presented in Rowe et al. (2019); below we provide summary information on the site and isotope analytical methods.

2.1. Study area

Girraween lagoon (−12.517656°S 131.080747°E; 25 masl) is a perennial freshwater waterbody, located on the outskirts of Darwin, Northern Territory, Australia. The site is currently ~30 km from the open ocean, but estuaries under tidal influence extend to within ~15 km of the site. The lagoon has a small catchment of 917 Ha exhibiting little relief. The lagoon itself has a surface area of 45 ha, and at the deepest point is about 4.5 m in the dry season. There is a wet season increase of ~1–2 m in water depth, with the lake surface in the wet season roughly coincident with the local water groundwater table.

The region experiences a strongly seasonal climate, encompassed within Köppen-Geiger's 'Tropical Savanna' classification subtype Aw (Peel et al., 2007). The mean annual temperature maximum is 32.6 °C (minimum 23.2 °C). In the strongly seasonal climate that characterises the study area, potential evaporation exceeds 1800 mm in most years (Charles et al., 2016) compared to mean annual regional rainfall of 1731 mm (Bureau of Meteorology Station 014015, Darwin Airport), with 90 % of rain falling in the wet season between November and April (Charles et al., 2016). Monsoon conditions are dominated by west to north-westerly winds whereas winds in the dry season are dominated by east to south-easterlies. The region is subject to Tropical Cyclones with records from 1964 to 2015 including 32 severe cyclone landfalls (categories 3, 4 or 5 on the Australian scale, BoM, 2017).

Modern vegetation around the site is *Eucalyptus*-dominated tropical open forest savanna and/or savanna woodland (dominant overstory species *Eucalyptus tetrodonta, Eucalyptus miniata, Corymbia polycarpa*) with a grassy understorey (Rowe et al., 2019). Variable transition communities dominated by *Lophostemon* spp. and *Melaleuca* spp. and broad-leaf herbs occur on approach to the water. The lagoon itself incorporates a wetland fringe, with zonations in vegetation close to the lagoon edge determined by depth of open water and extent of onshore soil waterlogging. *Melaleuca* form partly floating woodlands in the shallow waters and on waterlogged soils. A well-defined zone dominated by sedges rings the lagoon in shallow/seasonally flooded areas with *Nymphaea* and other submerged taxa occupying permanent open water.

Zwart et al. (2018) reported the daily oxygen and hydrogen isotope composition of rainfall in Darwin from 2014 to 2017, categorised into the five rainfall regimes of Pope et al. (2009) and Fig. 1. Half of total rainfall during the period was associated with the Deep West regime, characterised by large areas of deep convection and stratiform cloud, producing rainfall with low stable isotope values (weighted mean $\delta^2H = -44$ ‰). The remaining four regimes including the Shallow West and three Easterly regimes delivered the other half of total rainfall, with amount weighted mean values ranging from −26 to −5 ‰, none associated with large areas of stratiform rainfall. Zwart et al. (2018) also note that it is rainfall regime, not rainfall amount, that exerts the primary control on the stable isotope composition of rainfall, with daily rainfall amounts in excess of 100 mm having δ^2H values ranging widely from −100 to −6 ‰.

2.2. Field sampling

A 19.4 m core was collected from Girraween Lagoon using a floating platform with hydraulic coring-rig (Bird et al., 2024), with the focus of this paper being the upper 3.3 m. Each 1 m section was collected in plastic tubing and sealed in the field for transport. Core sections were split in half, described, and 66 samples taken at 5 cm intervals. The upper ~3.3 m that are the focus of this paper represent relatively uniform organic-rich sediments grading to organic-rich sediment with a higher proportion of fine clay below ~4 m depth (Rowe et al., 2019). The chronology is constrained in this interval by six radiocarbon dates and presented previously (Rowe et al., 2019; Sun et al., 2025).

2.3. Water isotope sampling and analysis

Accumulated 24-hourly rainfall was collected between 2014 and 2022 near Charles Darwin University (12.37°S 130.86°E), 28 km northwest of Girraween Lagoon. The stable isotope results to 2018 have previously been reported (Munksgaard et al., 2019; Zwart et al., 2018) with data up to 2022 ($n = 595$ in total) and all rainfall and lake isotope data are provided in Supplementary dataset 1. Girraween lagoon water from 30 cm depth was sampled monthly through 2017 into 50 ml Falcon plastic centrifuge tubes. Stable isotope analysis was carried out using Picarro L2120i and L2130i instruments and autosampler connected to a diffusion sampler device (see Munksgaard et al., 2011). Measurements were scaled relative to Vienna Standard Mean Ocean Water (V-SMOW) using three secondary water standards whose composition were determined relative to the certified isotope standards Vienna Standard Mean Ocean Water (V-SMOW), Standard Light Antarctic Precipitation (SLAP), and Greenland Ice Sheet Precipitation (GISP) by multiple analyses using Isotope Ratio Infrared Spectrometry and Isotope Ratio Mass Spectrometry at three laboratories. Precision is typically ±0.5 ‰ and ± 0.1 ‰ for δ^2H and $\delta^{18}O$, respectively (1σ).

2.4. Lipid extraction and analysis

Aliquots of 10–50 g of freeze-dried homogenised sediment were extracted in dichloromethane:methanol (9:1) at 100 °C for 15 min in a MARS 6 microwave digestion system. The resulting total lipid extract was dried under nitrogen and then transferred in hexane to a 4 ml glass vial. Alkanes were separated on a Restek 12 position solid-phase extraction (SPE) vacuum manifold using pre-cleaned 6 ml Chroma bond SPE glass columns (Macherey-Nagel) filled with 1.5 g of silica gel (0.040 mm to 0.063 mm mesh size). Extracts were transferred onto the column in hexane and eluted with a further 10 mL *n*-hexane. 10 μg of 5α-androstane (Sigma-Aldrich) was added as internal standard after SPE separation.

Sulphur was removed by loading the sample onto a long-stem glass pipette used as a column, half-filled with activated copper powder <425 μm (Sigma-Aldrich with a purity of 99.5 %). The copper was activated by washing with 6 ml of HCl and then rinsing with 10 ml Milli-Q water, followed by 6 ml acetone and 6 ml dichloromethane. Alkenes were removed with silver nitrate on silica gel (Sigma-Aldrich), activated in an oven at 105 °C for 1 h, packed into long stem glass pipettes ¾ full, and kept out of direct UV light. After cleaning the packed column with acetone, dichloromethane, and n-hexane, the sample was transferred in *n*-hexane onto the $AgNO_3$ column and eluted five times with *n*-hexane.

Branched alkanes were removed using urea adduction after drying of each sample into an 8 ml screw-top vial. Then, we added three solutions to the vial: (*i*) 300 μl 10 % urea solution (Ultra-Pure Urea >98 %;

Thermo-Fischer Scientific), (*ii*) 300 μl acetone, and (*iii*) 300 μl pentane (99 %; Scharlau). The vial was capped, the sample homogenised with a vortex mixer, placed into a freezer for 30 min, then evaporated to dryness under N_2. The urea crystallised as a precipitate with *n*-alkanes taken into channels in the urea structure while excluding branched alkanes. We rinsed the extract with 1 ml of *n*-hexane, leaving behind the clean urea crystals containing the *n*-alkanes. This procedure was repeated twice more. Then 500 μl of ultraclean HPLC Plus grade water (Sigma-Aldrich), 500 μl methanol, and 1.5 ml *n*-hexane was added to dissolve the urea. The immiscible *n*-hexane (containing the *n*-alkanes) was allowed to separate and then transferred into another 8 ml vial, repeated in tri. The entire process was repeated 4–5 more times to eliminate all branched alkanes.

Alkanes were identified and quantified on 1 μl aliquots using a Shimadzu QP2010 GC–MS equipped with a mass selective detector and a flame ionisation detector coupled via an electronic split interface. Quantification was enabled by reference to the peak area of the internal standard 5a-androstane. The GC–MS also enabled confirmation of the elimination of impurities. We determined the stable isotope composition ($\delta^{13}C$ and δ^2H values) of the purified *n*-alkanes in triplicate using a Trace 1310 gas chromatograph coupled to a Thermo-Scientific Delta V Plus isotope ratio mass spectrometer. The mass spectrometer measured the individual stable isotope composition of all *n*-alkanes present in sufficient quantity in each sample. The H_3^+ factor was evaluated every measurement sequence and was constant throughout the measurement period. Measured δ^2H values were converted to the isotopic water standard Vienna Standard Mean Ocean Water (VSMOW) scale by reference to a standard containing *n*-C_{16} to *n*-C_{30} alkanes (Mix A4, Arndt Schimmelmann, Indiana University) with known δ^2H values. Standards were measured in triplicate before and after each sample block containing five samples. $\delta^{13}C$ values previously reported in Hadeen et al. (2025) were similarly determined through reference to standards (Eicosane; Sigma-Aldrich, Androstane; Sigma-Aldrich, Docosane; Sigma-Aldrich, and Squalane; Alfa Aesar) on the international VPDB reference scale.

Hydrogen isotope data for all alkanes are presented in Supplementary Dataset 2. We aggregated the data as described in Hadeen et al. (2025), based on chain length distributions for 28 of the main aquatic and terrestrial species present in and around the lagoon. Each of these two alkanes is separated by a minimum of three carbon numbers (one odd carbon number) from the next group of two alkanes to minimise, but not eliminate, tailing of n-alkanes produced by one group into the next: (i) aquatic plants *n*-$C_{23–25}$ (δ^2H_{Aq}) with an average deviation from the mean of the two alkanes of ±4.2 ‰ for all samples ($n = 63$) (ii) terrestrial plants n-$C_{29–31}$ (δ^2H_{Te}; ± 3.2 ‰, $n = 66$) and (ii) sedges n-$C_{35–37}$ (δ^2H_{Se}; ± 6.2 ‰, n = 66).

Sachse et al. (2012) demonstrated that C_3 dicots, primarily trees ($\varepsilon_{C3} = -113$ ‰) fractionate hydrogen isotopes during the production of *n*-alkanes to a lesser degree than C_4 moncots, primarily grasses (average $\varepsilon_{C4} = -134$ ‰). Liu and An (2019) have further demonstrated that the difference between dicots and monocots is decreased at low latitudes with a dicot apparent ε_{C3} of −115 ‰ (range − 55 to −210 ‰) and monocot apparent ε_{C4} of −132 ‰ (range − 85 to −210 ‰). We use the values of Liu and An (2019) to calculate a net ε_{Te} between source water and alkanes for each δ^2H_{Te} value, recognizing that a significant range of values is reported for individual species and locations globally.

We use the $\delta^{13}C_{Te}$ for the same sample to calculate the fractions of C_3 and C_4 carbon contributing to the alkanes expressed as fC_4. We use the end-member values of −20.7 ± 0.7 ‰ for C_4 monocots (Sachse et al., 2012) and − 33.4 ± 0.4 ‰ for C_3 dicots (Garcin et al., 2014). Hattersley (1983) found that >90 % of the grass biomass in the region is produced by species that utilise the C_4 photosynthetic pathway, and this is unlikely to have changed over the course of the Holocene (Hadeen et al., 2025).

We then calculate the hydrogen isotope fractionation between the plant alkanes and their source water (ε_{Te}) and thereby the hydrogen isotope composition of the plant available moisture from which the alkanes were synthesised ($\delta^2H_{Te\text{-}P}$), as has been successfully applied in other tropical locations (Konecky et al., 2016).

$\varepsilon_{Te} = (fC_4 * \varepsilon_{Ce}) + ((1\text{-}fC_4) * \varepsilon_{C3})$.

$\delta^2H_{Te\text{-}P} = \{(\delta^2H_{Te} + 1000) / [(\varepsilon_{Te} /1000) +1]\} - 1000$.

We assume aquatic plants use the C_3 pathway and therefore apply ε_{C3}, to calculate $\delta^2H_{Aq\text{-}P}$ values and apply ε_{C4} to calculate $\delta^2H_{Se\text{-}P}$ values on the assumption that sedges, being monocots, fractionate hydrogen as would other monocots regardless of photosynthetic pathway. In addition, as a separate measure of C_3 and C_4 terrestrial plant abundance, we use grass (C_4) pollen as a proportion of total terrestrial pollen to calculate an f_{grass} value for use in calculating an alternative measure of $\delta^2H_{Te\text{–}P}$.

As defined by Hadeen et al. (2025) we calculate two indices designed to facilitate an assessment of the impact of *n*-alkane sources that, while producing *n*-alkane at highest abundance at higher or lower chain lengths, may contribute to some degree to the *n*-$C_{29–31}$ terrestrial plant group (and vice versa). These are:

Aq*(%) = [*n*-$C_{23–25}$ / (*n*-$C_{23–25}$ + *n*-$C_{29–31}$)] * 100.

Where *n*-$C_{23–25}$ is the relative abundance of *n*-alkanes primarily attributed to the aquatic plant group (and is equivalent to p_{aq}, except in units; Ficken et al., 2000) and *n*-$C_{29–31}$ is the relative abundance of *n*-alkanes primarily attributed to the terrestrial plant group, and,

Se*(%) = [*n*-$C_{35–37}$ / (*n*-$C_{35–37}$ + *n*-$C_{29–31}$)] * 100.

Where *n*-$C_{35–37}$ is the relative abundance of *n*-alkanes primarily attributed to the sedge plant group and *n*-$C_{29–31}$ is the relative abundance of *n*-alkanes primarily attributed to the terrestrial plant group.

3. Results

3.1. Water isotopes

The long term (February 2014 to March 2022) amount weighted mean δ^2H value of daily samples is −30.1 ‰ ($n = 595$), within the range of −26 to −34 ‰ calculated for the region in the Australia-wide study of Hollins et al. (2018). Modern rainfall, lake water depth and δ^2H variations all illustrate the strong seasonality of north Australia's climate (Fig. 2). In the two months preceding monsoon onset in late 2016, significant rainfall events of up to 129 mm occurred, associated with high δ^2H values of > + 4 ‰ (Supplementary data 1). These events did not result in an increase in lake level which remained low in January 2017. The monsoon began in late December in 2016 and eight heavy rainfall events with daily rainfall amounts of >100 mm, and up to 185 mm occurred from December 21st, 2016 to the end of April 2017. These events had δ^2H values from −28 to −101 ‰. Little rain was recorded outside this period through the rest of 2017 until November of that year, as is typical of the region (Fig. 2). The absence of rainfall in the dry season, while evapotranspiration fluxes were similar to the wet season (or higher, see Fig. 2), resulted in a ≈ 1 m decrease in lake water level over the year and a 30 ‰ progressive increase of δ^2H lake water values as a result of evaporation. Highest lake water δ^2H values were recorded in November 2017 (~0 ‰), before the following wet season of 2018.

3.2. Alkanes

The average *n*-alkane distribution from the Girraween lagoon samples in this study are shown in Fig. 3. They indicate a dominant higher plant source(s), with minor contributions from alkanes with a carbon number < *n*-C_{23}, increasing to a peak in relative abundance at *n*-C_{29}. The abundances of *n*-C_{31} and *n*-C_{33} are lower than *n*-C_{29}, but there is a second peak in abundance at *n*-C_{35} and n-alkanes occur in measurable quantities up to *n*-C_{39}.

Average chain lengths (ACL; calculated as in Hoffmann et al. (2013) eq. 1, using chain lengths from *n*-C_{19} to *n*-C_{19}) are initially ~28.5 at ~9.9 ka, rising steadily to a broad plateau from 2 to 5 ka with values between 31 and 32, thereafter decreasing to values of <32 toward the

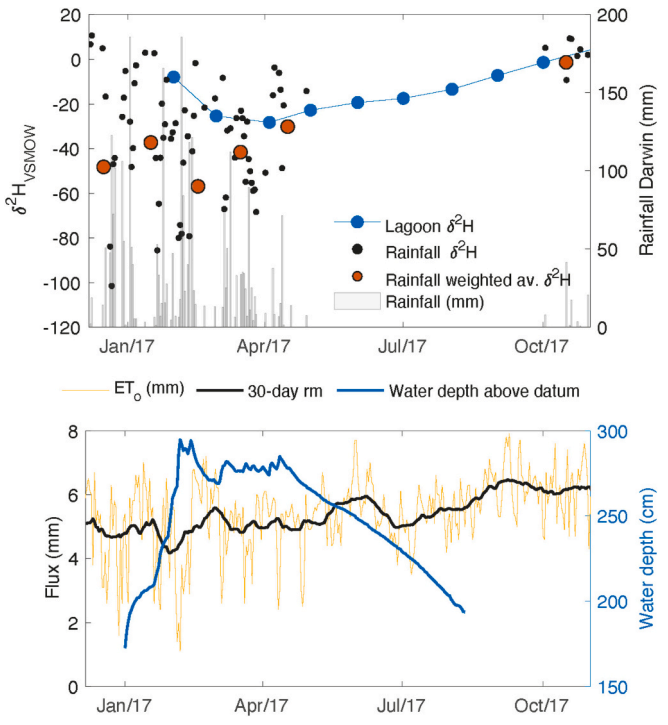

Fig. 2. Lagoon δ^2H values (blue dots), Daily rainfall δ^2H values (black dots) and monthly amount weighted δ^2H values (red dots). Rainfall amount is indicated by grey bars in the upper panel. Also shown in the lower panel is evaporative flux in mm (yellow), 30-day mean evaporative flux (black) and Water depth (blue). (For interpretation of the references to colour in this figure legend, the reader is referred to the web version of this article.)

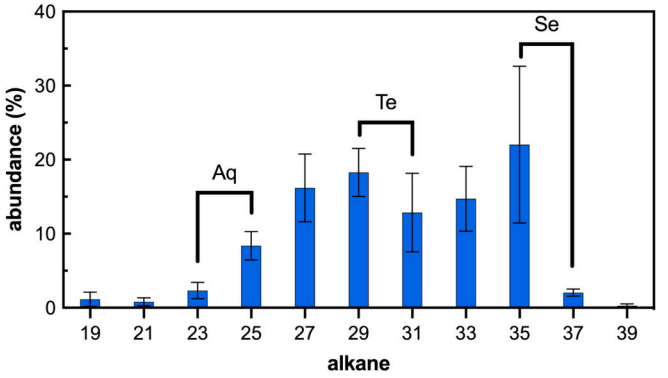

Fig. 3. Average n-alkane chain length distribution in all samples with 1 SD shown. Also shown are the alkane pairs used in the calculation of parameters for the aquatic (Aq), Terrestrial (Te) and Sedge (Se) groups.

present (Fig. 4C). Aq* values vary within a small range from ~20–30 %, while Se* values increase from 10 % to a broad peak of 50–65 % between 5 and 2 ka BP, decreasing to 30–50 % thereafter, closely mirroring the ACL record (Fig. 4C). The fC_4 calculated from the carbon isotope composition, is initially high at 0.95 then mirrors the decline in $\delta^{13}C$ values to a broad low of ~0.1 between 2.5 and 4.5 ka BP, followed by an increase to constant values of 0.2 after 1.5 ka BP. The fC_4 values are different from f_{grass} values, which instead decrease monotonically from ~84 % to ~40 % by 1 ka BP, thereafter rising again to 58 % toward the present (Fig. 4D).

The $\delta^{13}C$ values for the three n-alkane groups (Te, Aq and Se; Fig. 4B) range between −20.5 ‰ early in the record, decreasing to as low as −33 ‰ at ~3 ka BP, thereafter increasing to values of −29 to −30.3 ‰ in the surface samples. The δ^2H values for the three n-alkane groups (Te, Aq and Se; Fig. 4A) show broadly similar trends from relatively high values of −140 to −165 ‰ in the early Holocene, decreasing to −165 to −190 values between 45 and 5 ka until 2.5 ka. After 2.5 ka, δ^2H values decrease to a range generally between −160 and − 185 ‰ (Fig. 3). In general, δ^2H_{Se} values are lower, and δ^2H_{Aq} values higher, than δ^2H_{Te} values through most of the record with δ^2H_{Se} values diverging further from the other groups to lower values in the late Holocene.

The δ^2H values of plant available moisture (Fig. 5) are in closer accord with each other than the *n*-alkane values from which they are calculated, showing more divergence before 6 ka than after (Fig. 4). Initially, values range widely from −12 to −44 ‰ until ~5.5 ka, after which time they decrease to a broad plateau generally between −60 and − 80 ‰ between 2 and 4.7 ka. After 2 ka values become variable between −50 and − 64 ‰. In general, $\delta^2H_{Se\text{-}P}$ values are higher than $\delta^2H_{Te\text{-}P}$ values before 5 ka, similar from 5 to 1 ka and lower after that time. Conversely, $\delta^2H_{Aq\text{-}P}$ values are generally lower than $\delta^2H_{Te\text{-}P}$ values before 2.5 ka, becoming similar after that time.

3. Discussion.

3.3. Source water for the alkanes in Girraween lagoon

The calculated δ^2H_P values for the different plant groups in the recent past are relatively consistent, indicating modern plant available moisture (δ^2H_P) is in the range of −48 to −60 ‰ for all alkane groups (Fig. 5A). This is similar to range of −30 to −55 ‰ for monthly averaged wet season precipitation in 2017 (Fig. 2) and other wet seasons between 2014 and 2022, where the amount-weighted rainfall δ^2H was −44 ‰ for wet season rain associated with deep convection (Supplementary dataset 1). This suggests that wet season infiltration dominates plant water uptake and assimilation into the plant *n*-alkanes. We note that evaporation of the lake waters increases δ^2H into the dry season (Fig. 2), however our results were for surface samples that may not be representative of the entire water column occupied by aquatic biomass. The overall similarity between the trends for both aquatic and terrestrial species over time suggests that all plant groups access progressively more evaporated water over the course of a wet to dry season cycle; aquatics progressively more evaporated lake water and terrestrial species progressively more evaporated soil moisture.

The agreement between modern calculated δ^2H_P and observed modern rainfall δ^2H values is not perfect because we use the low latitude mean ε_{app} values (Liu and An, 2019). That synthesis reports a range in ε_{app} values from −210 ‰ to −48 ‰ for dicots and − 212 ‰ to −49 ‰ for monocots at the global scale. Empirical data is sparse for Australia. Kahmen et al. (2013) demonstrated that biosynthetic fractions in two dominant tree genera - *Eucalyptus* and *Acacia* - in the current study region and south on a transect of increasing aridity, were different from each other (−183 and − 133 ‰ respectively) and also that ε_{app} values for both genera are sensitive to aridity. Li et al. (2024) calculated ε_{app} values for eleven C_4 grass species in tropical Australia that ranged from −161 to −205 ‰. These Australian values are all higher than the low latitude end-member mean values of Liu and An (2019) assumed in this study ($\varepsilon_{C3} = -115$ ‰ and $\varepsilon_{C4} = -132$ ‰), and this is likely the reason for the comparatively lower calculated δ^2H_P values.

We do not attempt to modify the end-member ε_{app} values so that δ^2H_P values are in better accord with modern observations, because there is insufficient basis upon which to identify more appropriate local values, and these may have changed over time. Instead, we interpret the trends in the record, cognizant of the fact that multiple factors can influence the hydrogen-isotope composition of both the plant available moisture, and the *n*-alkanes synthesised from that water. These include changes in the source, amount, mechanism of condensation and seasonal distribution of rainfall arriving at the site (Zwart et al., 2018). They also include, as discussed above, a number of species-, and therefore location-specific variables that govern the apparent water-alkane isotope fractionation factor (ε_{app}).

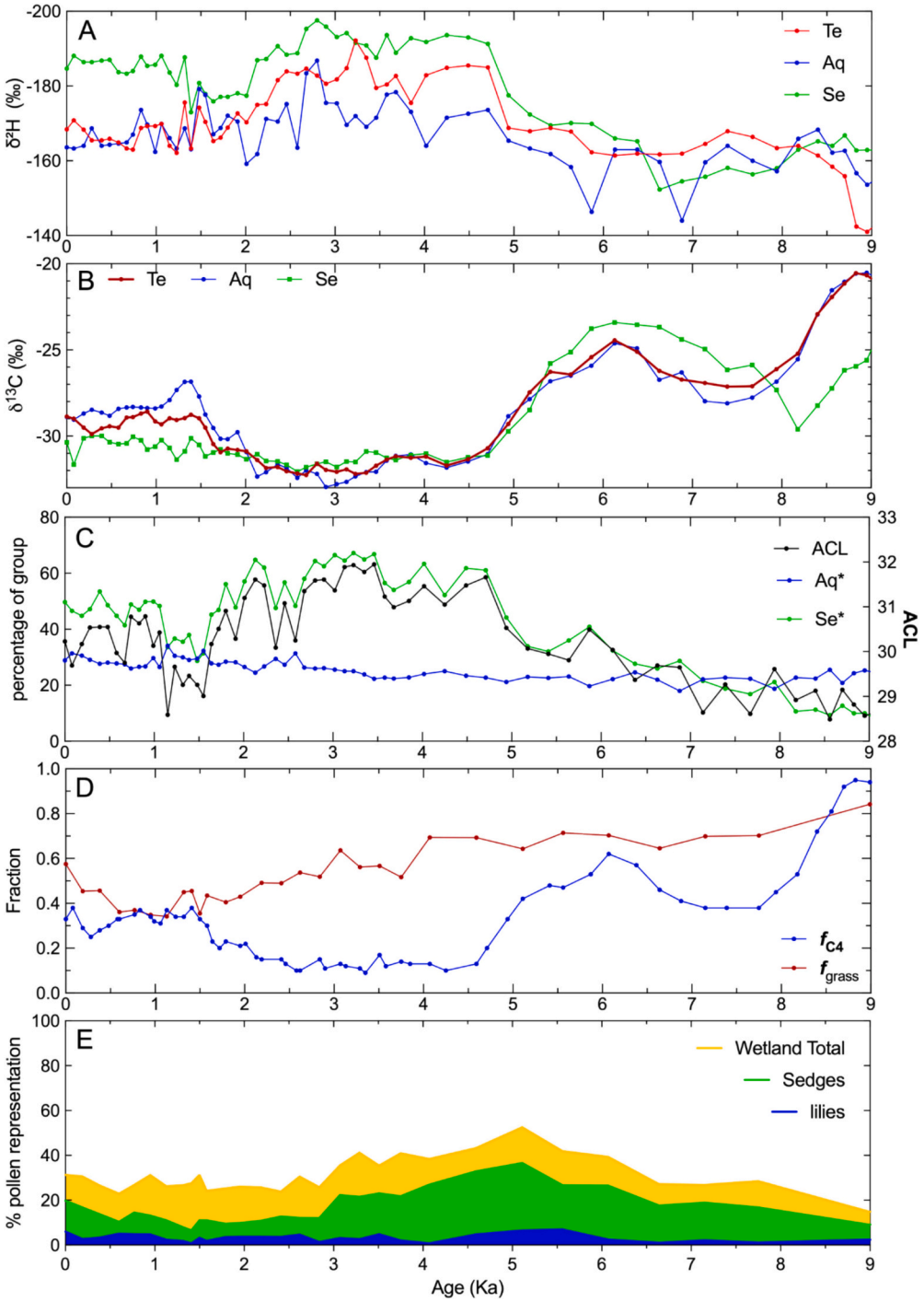

Fig. 4. Proxy records from Girraween Lagoon spanning the last 9 ka. **A:** Hydrogen isotope composition of n-alkanes attributed to the Terrestrial (Te), Aquatic (Aq) and sedge (Se) groups. Note x-axis is inverted, so 'wetter' is up. **B:** Carbon isotope composition of n-alkanes attributed to the Terrestrial (Te), Aquatic (Aq) and sedge (Se) groups. **C:** Average Chain length (ACL) and proportion of Aquatic (Aq*) and Sedge (Se*) alkanes calculated as explained in section 2.4. **D:** Grass pollen as a fraction of total dryland pollen (f_{grass}) and fraction of C_4 carbon (fC_4) calculated as described in section 2.4. **E:** percentage of wetland pollen in the total pollen spectra, and the separate contribution of sedge and lily pollen to the wetland pollen count (from Rowe et al., 2019). Modelled age uncertainties from the radiocarbon chronology increase to ±0.1 ka over 0–2 ka and then to ±0.2 ka by 9 ka.

3.4. Comparison with regional records

The Girraween site is in the core monsoon region of Northern Australia (Suppiah, 1992), with rainfall during the core monsoon season dominantly associated with the Deep West rainfall regime, and subordinate amounts derived from the west, east and southeast both during and outside the monsoon season (Zwart et al., 2018; Fig. 1). There are two terrestrial records in the immediate region of similar length and sufficient resolution to enable direct comparison with the Girraween n-alkane record:

(i) the KNI-51 speleothem record is located 300 km south (and 200 km west) of Girraween lagoon. It is currently close to the southern boundary of the ITCZ as defined by high-reflective cloud analysis (Denniston et al., 2016), and in the 'pseudo-monsoon' domain (Fig. 1)

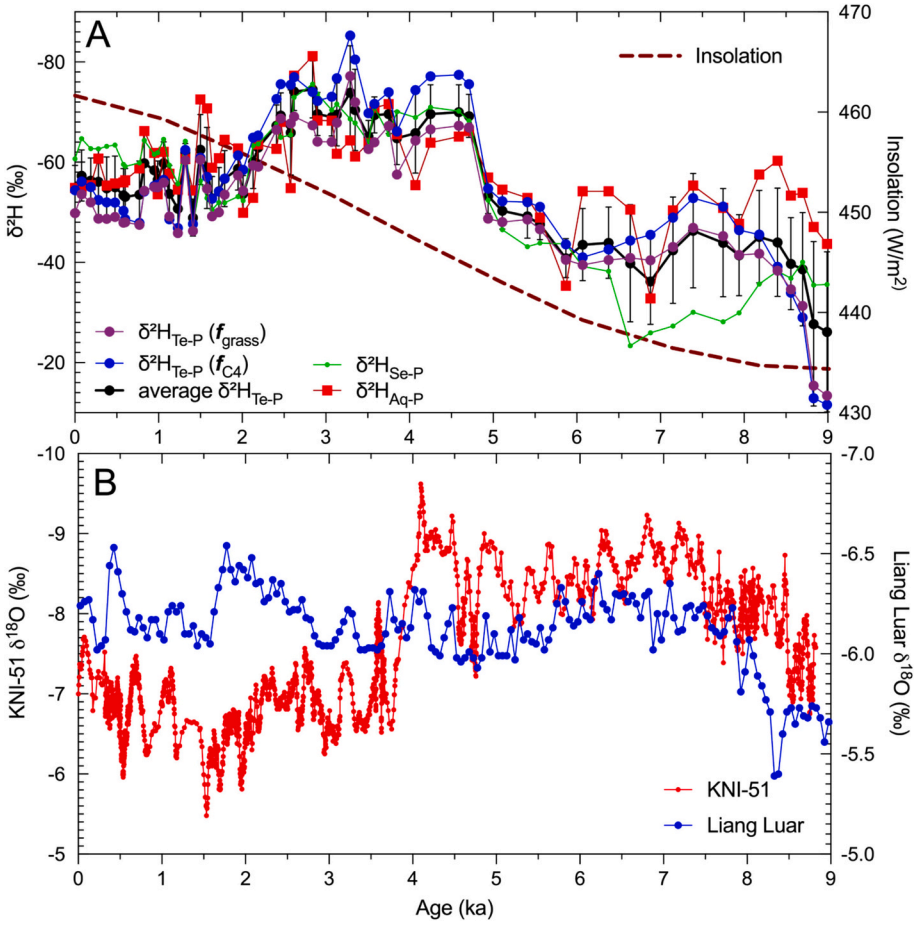

Fig. 5. Comparison between the Girraween and speleothem isotope records, locations shown on Fig. 1. **A:** Hydrogen isotope of plant available moisture for different plant groups, calculated as described in section 2.4, with the amount-weighted hydrogen isotope composition of modern precipitation indicated by 'P' and the horizontal dashed line, austral summer insolation for the latitude and longitude of the site also shown. **B:** Oxygen isotope records for speleothems from KNI-51 (Denniston et al., 2013a) and Liang Luar (Scroxton et al., 2022). In both panels, the y-axes for isotope measurements have been reversed, so 'wetter' conditions are toward the top of the panel. Modelled age uncertainties from the radiocarbon chronology increase to ±0.1 ka over 0–2 ka and then to ±0.2 ka by 9 ka.

where westerly airflow is sourced in the mid-latitudes and traverses the Indian Ocean, rather than tropical areas the north (Suppiah, 1992). Annual rainfall is 838 mm (Denniston et al., 2013a, 2013b), around half that at Girraween, concentrated in the single monsoon season and subject to significant inter-annual variability.

(ii) the Liang Luar speleothem record (Ayliffe et al., 2013; Scroxton et al., 2022) is located on the island of Flores 400 km north (and 1200 km west) of Girraween Lagoon, in the core monsoon region. Annual rainfall is ~1600 mm, similar to Girraween Lagoon, but distributed over a longer period between October and May as the ITCZ passes south, then north over the island through the monsoon season (Scroxton et al., 2022).

These three records provide the opportunity to examine both spatial and temporal aspects of monsoon evolution over the last 9 ka, in a relatively constrained region toward the southern limit of the modern ITCZ. This is important because the tropical rainbelt, as defined by the ITCZ, can potentially (i) change intensity (produce more or less precipitation in the rainbelt itself), (ii) move to a more southerly or northerly position, and/or (iii) expand or contact in latitudinal extent (Denniston et al., 2016). Depending on these dynamics, a proxy response that is interpreted as a change in rainfall at different locations in the same general region will potentially be quite different and occur with differing timings. It is also the case that wider coupling from northern Australia to other global climate drivers may vary in strength (McRobie et al., 2015), so significant correlations with distant records are not necessarily always to be expected.

At 9 ka δ^2H_P values at Girrwaeen were the highest in the record, indicating relatively drier than modern conditions and implying a less intense monsoon, consistent with low insolation (Fig. 5). This inference is supported by relatively low wetland pollen representation (indicating lower water level; Fig. 4E), low Se* values indicating reduced shallow water and adjacent dampland area suitable for sedge colonisation (Hadeen et al., 2025) and an extensive very open grassy savanna beyond the lagoon (Fig. 4C and D). Both the Liang Luar and KNI-51 speleothem records (Fig. 5), similarly suggest relatively dry conditions at this time. An increase in monsoon rainfall, implying an expansion of ITCZ area and southward shift of the southern boundary of the ITCZ is evident in all three records between 9 ka and 7.5–8 ka. At Girraween lagoon, this inference is also supported by increased wetland pollen representation and to a lesser extent Se*, along with a trend to increased woodiness in the surrounding savanna.

All three records indicate a period of wetter, stable conditions, as insolation increased toward the mid-Holocene between 6 and 8 ka. This period is recognized in northern Australia as a wet period (Denniston et al., 2013a) and globally as a period of reduced ENSO variability (McGregor et al., 2013; Leonard et al., 2016; White et al., 2018). More southerly penetration of the ITCZ is likely to have brought the KNI-51 into the core monsoon region, hence the relatively consistent trends between the three records into the mid-Holocene. McRobie et al. (2015) identify global scale couplings between the Australian summer monsoon and distant proxy records, implying global scale forcing, characterises the early to middle Holocene. This implies that at the regional scale

under consideration here, proxy records should exhibit some coherence at this time.

A significant decrease in δ^2H_P values occurs in the Girraween record between 4.5 and 5 ka, coincident with a further increase in Se*, and therefore in ACL (Fig. 4C) and highest wetland pollen representation (Fig. 4E) indicating an increase in shallow water area and seasonal dampland suitable for sedge colonisation. A decrease in $\delta^{18}O$ values, indicating wetter conditions, is also evident to some extent in the KNI-51 record between 4 and 5 ka, but not in the Liang Luar record. The period from 2.5 to 4.5 ka marks the time of maximum monsoon rainfall at Girraween lagoon, with δ^2H_P values decreasing to −60 to −80 ‰, indicating that the bulk of rainfall is consistently associated with the Deep West regime, derived from large areas of deep convection. This is suggestive of a further southward displacement of the ITCZ into northern Australia. The higher resolution, more southerly KNI-51 record, toward the limit of the ITCZ reveals further variability, suggesting short term variations in the southern limit of the ITCZ not visible in the Girraween record in the core monsoon domain. Nott and Price (1994, 1999) have previously identified 3.6 to 8 ka as the period of maximum monsoon rainfall from thermoluminescence dating of plunge pool deposits, all within a 200 km radius of Girraween lagoon, with the youngest age revised by May et al. (2015) to 2.9 ka, consistent with the Girraween record.

After 4 ka, the KNI-51 record diverges from both the Girraween and Liang Luar records. The KNI-51 record suggests a rapid decrease in rainfall between 4 ka and 3.5 ka, whereas there is little change evident in either the Girraween or Liang Luar records. This is consistent with a northward movement or contraction of the ITCZ that began by 4 ka, and wetland pollen representation at Girraween was also declining slightly (Fig. 4E) implying a trend to lower rainfall may already have been underway at Girraween that is not evident in the hydrogen isotope record. At 2.5–3 ka, despite an ongoing increase in insolation, a second decrease in rainfall in evident in the KNI-51 record, that is mirrored in a sustained increase in δ^2H_P values in the Girraween record, and an increase in rainfall in the Liang Luar record. In all locations this change is complete by 1.5 ka. These characteristics imply a further northward retreat of the ITCZ, reducing rainfall and/or reducing the proportion of rain associated with the Deep West rainfall regime at Girraween and KNI-51, but leading to increasing rainfall further north at Liang Luar. The last 1.5 ka are characterised at Girraween lagoon by stable δ^2H_P values, lower than before 5 ka, stable wetland pollen representation implying stable lagoon water level, lower than during the mid-Holocene and a small increase in savanna woodiness. KNI-51 exhibits an overall wetting trend and Liang Luar, invariant rainfall, except for brief wetter period centred on 0.5 ka.

The period from 5 to ~3 ka is clearly identifiable as the time of peak monsoon intensity associated with an increased influence of the Deep West rainfall regime, consistently delivering precipitation with low δ^2H_P values to the Girraween area and leading to consistently high lake levels. Both the Liang Luar record and a marine record of terrestrial runoff nearby (Steinke et al., 2014a, 2014b) identifies ~3–6 ka as a time of decreased monsoon intensity in Southern Indonesia, indicating that the ITCZ moved to a more southerly position during this time.

Equally clearly, the period from 2.5 to 3 ka marks a sustained regional shift in monsoon dynamics continued to the present, either in the source or amount of rainfall (or both) at Girraween Lagoon, and Steinke et al. (2014a, 2014b) marks 2.8 ka as the time when the monsoon intensified in southern Indonesia, a shift in ITCZ mean position to the north, away from northern Australia. This shift cannot simply be explained by insolation, which continues to increase toward the present. McRobie et al. (2015) notes that from 3 ka, the KNI-51 record becomes decoupled from global drivers, and is only correlated with the Laguna Pallacocha ENSO record (Moy et al., 2002; Mark et al., 2022). This suggests that an ENSO teleconnection becomes more important as a driver of northwest Australian rainfall. It is well established that ENSO cyclicity was reduced in the mid-Holocene (Conroy et al., 2008), and increased ENSO variability in the late Holocene has been suggested in several studies (Conroy et al., 2008; Denniston et al., 2013; Mark et al., 2022). In the northern Australia region this change began at 4 ka in the KNI-51 area and was evident in the core monsoon Girraween area after 3 ka.

3.5. ENSO variability

Monsoon rainfall in northwestern Australia is currently influenced by ENSO such that lower rainfall, including during the pre-monsoon months from September characterises El Niño events and enhanced rainfall, including the pre-months from September, characterises La Niña events (Heidemann et al., 2023). This influence obviously extends back in time, and the Girraween records compared here suggest that this influence may have been established, at 2.5–3 ka. Clearly ENSO is not the only climate phenomenon capable of influencing regional monsoon dynamics, with Indian Ocean Sea surface temperatures, the Indian Ocean dipole, the Pacific Decadal Oscillation, the Madden Julian Oscillation, terrestrial processes associated with soil moisture and internal atmospheric variability all contributing to monsoon variability on a range of timescales (Heidemann et al., 2022). However, the timing of the changes observed in the Girraween record and the timing of increased ENSO impact on hydroclimate as inferred from remote proxy records (Moy et al., 2002; Conroy et al., 2008) does suggest an increased ENSO influence on monsoon dynamics as the overarching cause for the ~10–15 ‰ increase in δ^2H_P values in the Girraween record after 2.5–3 ka. Denniston et al. (2013) has previously suggested increased influence of ENSO on monsoon dynamics from 4 ka based on the KNI-51 record.

The inference and timing of the change to increased ENSO variability correlates well with other records in northern Australia and elsewhere, which are generally placed between 4 and 3 ka (Woodroffe and Gagan, 2000; Denniston et al., 2013a, 2013b; Barr et al., 2019; White et al., 2018). Wurster et al. (2021) also note 3 ka as the time that fire regime around Girraween lagoon changed, attributed in that study to increased ENSO variability.

If ENSO is at least in part influencing hydroclimate as inferred from the Girraween and speleothem records, then ENSO must be able to influence the isotope composition of monsoon rainfall. Monthly stable isotope measurements of Darwin rainfall by the International Atomic Energy Agency began in 1979. The data is incomplete but is augmented by the daily data presented here from 2014, enabling an assessment of the stable isotope composition of rainfall during four El Niño and four La Niña events. Fig. 6 demonstrates that δ^2H values of precipitation during El Niño events is significantly higher ($p = 0.035$), by an average of ~13 ‰, and up to 31 ‰, than during La Niña events (see Supplementary Table 1 for summary statistics). The same is true for $\delta^{18}O$ values, with precipitation during El Niño events on average ~ 1.8 ‰, and up to 4 ‰ ($p = 0.026$), higher than during La Niña events. A significant negative relationship between $\delta^{18}O$ values and Southern Oscillation Index has also previously been identified using the IAEA data for multiple locations across the EASM-IASM monsoon domain (Zhang et al., 2022).

The comparison in Fig. 6 is between the two extremes of ENSO cyclicity, so the difference places an indication of the impact of ENSO variability on the stable isotope composition of precipitation, and ~ 13 ‰ is smaller than the observed change in the Girraween record. The additional difference is likely the result of two things: (i) it is likely that increased evaporative modification of precipitation isotope composition in the soil and lake waters during drier El Niño phases also contributes to the change in δ^2H_P values after 2.5–3 ka, and (ii) It is also likely that a sustained decrease in the proportion of deep convective rainfall associated with the Deep West rainfall regime and therefore an increase in the proportion of rainfall derived from other rainfall regimes that deliver rainfall with a higher hydrogen isotope composition, particularly the Shallow West regime associated with the westerly wind bursts associated with monsoon onset on the Girraween area, and therefore moisture source area, may have contributed to the observed increase in δ^2H_P values after 2.5–3 ka at Girraween Lagoon.

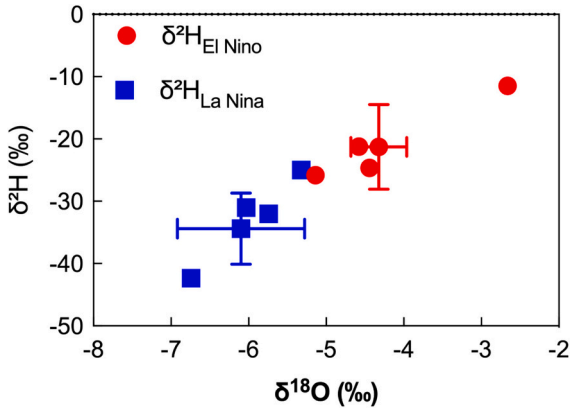

Fig. 6. Annual amount-weighted mean stable isotope composition of Darwin rainfall during La Niña (Low SOI) and El Niño (High SOI) years as identified by Southern Oscillation Index (from https://psl.noaa.gov/data/climateindices/) and for which full data was available from the IAEA, Munksgaard et al. (2019) and this study from 1979 to 2022. Mean for each also shown with the error shown being average deviation from the mean of the results for individual years.

4. Conclusions

The Girraween record is a lower resolution, mutli-proxy, record that can be directly compared to the higher resolution, but single proxy, records from speleothems in the same broad region. This enables a nuanced understanding of both the spatial and temporal dynamics of the ITCZ and associated rainfall over the Holocene within the southern IASM monsoon domain. The results highlight the fact that because the ITCZ can intensify, expand and move latitudinally (Denniston et al., 2016), records from different, even relatively close locations will not necessarily respond in the same way at the same time. Even at relatively regional scales it is 'more complicated than that' (Scott, 2001).

All three records record an initial period of monsoon intensification between ~7.5 and 9 ka, but after this time the responses of the three records diverge. The KNI-51 record is currently south of the zone of maximum rainfall in northern Australia (Kuhnt et al., 2015; Denniston et al., 2023). The trends in the KNI-51 record tend to be anti-correlated with the Liang Luar (Denniston et al., 2013a, 2013b and Fig. 5B), north of the zone of maximum rainfall during monsoon conditions in northern Australia (Denniston et al., 2023), particularly before ~4 ka. This anti-correlation may be be linked to small shifts northward or southward the mean position of the ITCZ over time, but are not visible in the Girraween record because (i) the record is of lower resolution and (ii) the site is located within the region of maximum rainfall in northern Australia and is therefore less sensitive to changes in mean ITCZ position.

The Girraween record clearly demonstrates a period of particularly enhanced monsoon, likely the result of a dominance of rainfall from the Deep West regime at the site between 5 ka and ~ 3 ka, relating to a southerly shift in mean ITCZ position which resulted in a reduction in rainfall in southern Indonesia (Steinke et al., 2014a, 2014b; Ayliffe et al., 2013). This enhancement was also recorded at the KNI-51 but only persisted until 4 ka, implying a weakening in monsoon intensity further south at the KNI-51 site that did not impact the Girraween site. Continued movement of the ITCZ to a more northerly position was augmented by stronger ENSO teleconnections initiated at 2–5-3 ka. Northerly movement of mean ITCZ position led to a reduction in monsoon intensity at both Girraween and KNI-1 and an increase in monsoon strength in southern Indonesia. The configuration established at the time has been broadly sustained to the present as evidenced by the Girraween record although the higher resolution KNI-51 and Liang Luar records do indicate periods of enhanced and reduced monsoon intensity during this time that are not evident in the Girraween record.

Supplementary data to this article can be found online at https://doi.org/10.1016/j.palaeo.2025.113094.

Contributions

MIB, CMW, and CR designed the study. MIB, CR, CMW, MB, RC, XH, and CZ did field sampling and initial preparation, NM and CZ did the water isotope analyses, XH the compound specific isotope analyses, CR the palynology. All authors contributed to the interpretation and the final form of the manuscript.

CRediT authorship contribution statement

Michael I. Bird: Writing – review & editing, Writing – original draft, Supervision, Project administration, Methodology, Investigation, Funding acquisition, Formal analysis, Data curation, Conceptualization. **Michael Brand:** Methodology, Investigation. **Rainy Comley:** Writing – review & editing, Methodology, Investigation. **Xennephone Hadeen:** Writing – review & editing, Methodology, Investigation, Formal analysis. **Niels C. Munksgaard:** Visualization, Methodology, Investigation, Formal analysis. **Cassandra Rowe:** Writing – review & editing, Visualization, Methodology, Investigation, Formal analysis, Conceptualization. **Christopher M. Wurster:** Writing – review & editing, Methodology, Investigation. **Costijn Zwart:** Writing – review & editing, Methodology, Investigation, Formal analysis.

Declaration of competing interest

The authors declare no conflict of interest.

Data availability

all data is available in the supplementary files

Acknowledgements

This research was funded by the Australian Research Council Centre of Excellence for Australian Biodiversity and Heritage (CE170100015), the Australian Research Council Centre of Excellence for Indigenous and Environmental Histories and Futures (CE230100009) and an Australian Research Council Laureate Fellowship to M.I·B (FL140100044). C. Zwart acknowledges receipt of an Australian Postgraduate Award. We thank Larrakia and Wulna Traditional Owners for permission to do this research on their traditional lands.

References

Ayliffe, L.K., Gagan, M.K., Zhao, J.X., Drysdale, R.N., Hellstrom, J.C., Hantoro, W.S., Griffiths, M.L., Scott-Gagan, H., St Pierre, E., Cowley, J.A., Suwargadi, B.W., 2013. Rapid interhemispheric climate links via the Australasian monsoon during the last deglaciation. Nat. Commun. 4, 2908.

Barr, C., Tibby, J., Leng, M.J., Tyler, J.J., Henderson, A.C.G., Overpeck, J.T., Simpson, G. L., Cole, J.E., Phipps, S.J., Marshall, J.C., McGregor, G.B., 2019. Holocene el Niño–Southern Oscillation variability reflected in subtropical Australian precipitation. Sci. Rep. 9 (1), 1627.

Bird, M.I., Brand, M., Comley, R., Fu, X., Hadeen, X., Jacobs, Z., Rowe, C., Wurster, C.M., Zwart, C., Bradshaw, C.J., 2024. Late Pleistocene emergence of an anthropogenic fire regime in Australia's tropical savannahs. Nat. Geosci. 17 (3), 233–240.

Bureau of Meteorology (BoM), 2017. Weather and climate Data. Commonwealth of Australia. http://www.bom.gov.au/climate/data/ (Accessed May 2018).

Caley, T., Malaizé, B., Revel, M., Ducassou, E., Wainer, K., Ibrahim, M., Shoeaib, D., Migeon, S., Marieu, V., 2011. Orbital timing of the Indian, East Asian and African boreal monsoons and the concept of a 'global monsoon'. Quat. Sci. Rev. 30 (25–26), 3705–3715.

Charles, S., Petheram, C., Berthet, A., Browning, G., Hodgson, G., Wheeler, M., Yang, A., Gallant, S., Marshall, A., Hendon, H., Kuleshov, Y., Dowdy, A., Reid, P., Read, A., Feikema, P., Hapuarachchi, P., Smith, T., Gregory, P., Shi, L., 2016. Climate data and their characterisation for hydrological and agricultural scenario modelling across the Fitzroy, Darwin and Mitchell catchments. In: A Technical Report from the CSIRO Northern Australia Water Resource Assessment to the Government of Australia. CSIRO, Australia.

Chen, J., Rao, Z., Liu, J., Huang, W., Feng, S., Dong, G., Hu, Y., Xu, Q., Chen, F., 2016. On the timing of the East Asian summer monsoon maximum during the Holocene—does the speleothem oxygen isotope record reflect monsoon rainfall variability? Sci. China Earth Sci. 59 (12), 2328–2338.
Conroy, J.L., Overpeck, J.T., Cole, J.E., Shanahan, T.M., Steinitz-Kannan, M., 2008. Holocene changes in eastern tropical Pacific climate inferred from a Galápagos lake sediment record. Quat. Sci. Rev. 27 (11–12), 1166–1180.
Cook, G.D., Heerdegen, R.G., 2001. Spatial variation in the duration of the rainy season in monsoonal Australia. Int. J. Climatol. 21 (14), 1723–1732.
D'Arrigo, R., Baker, P., Palmer, J., Anchukaitis, K., Cook, G., 2008. Experimental reconstruction of monsoon drought variability for Australasia using tree rings and corals. Geophys. Res. Lett. 35 (12).
Denniston, R.F., Wyrwoll, K.H., Polyak, V.J., Brown, J.R., Asmerom, Y., Wanamaker Jr., A.D., LaPointe, Z., Ellerbroek, R., Barthelmes, M., Cleary, D., Cugley, J., 2013a. A stalagmite record of Holocene Indonesian–Australian summer monsoon variability from the Australian tropics. Quat. Sci. Rev. 78, 155–168.
Denniston, R.F., Asmerom, Y., Lachniet, M., Polyak, V.J., Hope, P., An, N., Rodzinyak, K., Humphreys, W.F., 2013b. A last Glacial Maximum through middle Holocene stalagmite record of coastal Western Australia climate. Quat. Sci. Rev. 77, 101–112.
Denniston, R.F., Ummenhofer, C.C., Wanamaker, A.D., Lachniet, M.S., Villarini, G., Asmerom, Y., Polyak, V.J., Passaro, K.J., Cugley, J., Woods, D., Humphreys, W.F., 2016. Expansion and contraction of the Indo-Pacific tropical rain belt over the last three millennia. Sci. Rep. 6 (1), 34485.
Denniston, R.F., Asmerom, Y., Polyak, V.J., Wanamaker Jr., A.D., Ummenhofer, C.C., Humphreys, W.F., Cugley, J., Woods, D., Lucker, S., 2017. Decoupling of monsoon activity across the northern and southern Indo-Pacific during the late Glacial. Quat. Sci. Rev. 176, 101–105.
Denniston, R.F., Ummenhofer, C.C., Emanuel, K., Ingrosso, R., Pausata, F.S., Wanamaker, A.D., Lachniet, M.S., Carr, K.T., Asmerom, Y., Polyak, V.J., Nott, J., 2023. Sensitivity of northwest Australian tropical cyclone activity to ITCZ migration since 500 CE. Sci. Adv. 9 (2) eadd9832.
Dey, R., Lewis, S.C., Arblaster, J.M., Abram, N.J., 2019. A review of past and projected changes in Australia's rainfall. Wiley Interdiscip. Rev. Clim. Chang. 10 (3), e577.
Du, X., Russell, J.M., Liu, Z., Otto-Bliesner, B.L., Gao, Y., Zhu, C., Oppo, D.W., Mohtadi, M., Yan, Y., Galy, V.V., He, C., 2021. Deglacial trends in Indo-Pacific warm pool hydroclimate in an isotope-enabled Earth system model and implications for isotope-based paleoclimate reconstructions. Quat. Sci. Rev. 270, 107188.
Ficken, K.J., Li, B., Swain, D.L., Eglinton, G., 2000. An n-alkane proxy for the sedimentary input of submerged/floating freshwater aquatic macrophytes. Org. Geochem. 31 (7–8), 745–749.
Field, E., McGowan, H.A., Moss, P.T., Marx, S.K., 2017. A late Quaternary record of monsoon variability in the Northwest Kimberley, Australia. Quat. Int. 449, 119–135.
Garcin, Y., Schwab, V.F., Gleixner, G., Kahmen, A., Todou, G., Séné, O., Onana, J.M., Achoundong, G., Sachse, D., 2012. Hydrogen isotope ratios of lacustrine sedimentary n-alkanes as proxies of tropical African hydrology: insights from a calibration transect across Cameroon. Geochim. Cosmochim. Acta 79, 106–126.
Garcin, Y., Schefuß, E., Schwab, V.F., Garreta, V., Gleixner, G., Vincens, A., Todou, G., Séné, O., Onana, J., Achoundong, G., Sachse, D., 2014. Reconstructing C3 and C4 vegetation cover using n-alkane carbon isotope ratios in recent lake sediments from Cameroon, Western Central Africa. Geochim. Cosmochim. Acta 142, 482–500.
Griffiths, M.L., Drysdale, R.N., Gagan, M.K., Zhao, J.X., Ayliffe, L.K., Hellstrom, J.C., Hantoro, W.S., Frisia, S., Feng, Y.X., Cartwright, I., Pierre, E.S., 2009. Increasing Australian–Indonesian monsoon rainfall linked to early Holocene sea-level rise. Nat. Geosci. 2 (9), 636.
Hadeen, X., Rowe, C., Brand, M., Comley, R., Das, S., Wurster, C.M., Zwart, C., Bird, M.I., 2025. Comparing pollen and n-alkane carbon isotope records in a tropical lacustrine environment. Quat. Sci. Rev. 351, 109204.
Haig, J., Nott, J., Reichart, G.J., 2014. Australian tropical cyclone activity lower than at any time over the past 550–1,500 years. Nature 505 (7485), 667.
Hattersley, P.W., 1983. The distribution of C3 and C4 grasses in Australia in relation to climate. Oecologia 57, 113–128.
Heidemann, H., Cowan, T., Henley, B.J., Ribbe, J., Freund, M., Power, S., 2023. Variability and long-term change in Australian monsoon rainfall: a review. Wiley Interdiscip. Rev. Clim. Chang. 14 (3), e823.
Heidemann, H., Cowan, T., Henley, B.J., Ribbe, J., Freund, M., Power, S., 2023. Variability and long-term change in Australian monsoon rainfall: A review. Wiley Interdisciplinary Reviews: Climate Change 14 (3), e823.
Hoffmann, B., Kahmen, A., Cernusak, L.A., Arndt, S.K., Sachse, D., 2013. Abundance and distribution of leaf wax n-alkanes in leaves of Acacia and Eucalyptus trees along a strong humidity gradient in northern Australia. Org. Geochem. 62, 62–67.
Hollins, S.E., Hughes, C.E., Crawford, J., Cendón, D.I., Meredith, K.M., 2018. Rainfall isotope variations over the Australian continent–Implications for hydrology and isoscape applications. Sci. Total Environ. 645, 630–645.
Hung, C.W., Yanai, M., 2004. Factors contributing to the onset of the Australian summer monsoon. Q. J. R. Meteorol. Soc. 130 (597), 739–758.
Ishiwa, T., Yokoyama, Y., Reuning, L., McHugh, C.M., De Vleeschouwer, D., Gallagher, S. J., 2019. Australian Summer Monsoon variability in the past 14,000 years revealed by IODP Expedition 356 sediments. Prog Earth Planet Sci 6 (1), 17.
Kahmen, A., Hoffmann, B., Schefuß, E., Arndt, S.K., Cernusak, L.A., West, J.B., Sachse, D., 2013. Leaf water deuterium enrichment shapes leaf wax n-alkane δD values of angiosperm plants II: Observational evidence and global implications. Geochim. Cosmochim. Acta 111, 50–63.
Kiem, A.S., Johnson, F., Westra, S., van Dijk, A., Evans, J.P., O'Donnell, A., Rouillard, A., Barr, C., Tyler, J., Thyer, M., Jakob, D., 2016. Natural hazards in Australia: droughts. Clim. Chang. 139 (1), 37–54.
Konecky, B., Russell, J., Bijaksana, S., 2016. Glacial aridity in Central Indonesia coeval with intensified monsoon circulation. Earth Planet. Sci. Lett. 437, 15–24.
Kuhnt, W., Holbourn, A., Xu, J., Opdyke, B., De Deckker, P., Röhl, U., Mudelsee, M., 2015. Southern Hemisphere control on Australian monsoon variability during the late deglaciation and Holocene. Nat. Commun. 6 (1), 5916.
Lachniet, M.S., 2009. Climatic and environmental controls on speleothem oxygen-isotope values. Quat. Sci. Rev. 28 (5–6), 412–432.
Leonard, N.D., Welsh, K.J., Lough, J.M., Feng, Y.X., Pandolfi, J.M., Clark, T.R., Zhao, J. X., 2016. Evidence of reduced mid-Holocene ENSO variance on the Great Barrier Reef. Australia. Paleoceanography 31 (9), 1248–1260.
Li, T., Zhou, Y., Wurster, C.M., Zhou, X., Comely, R., Munksgaard, N.C., Cernusak, L.A., Haig, J., Bird, M.I., 2024. Vegetation and precipitation change inferred from the $\delta^{13}C$ and $\delta^{2}H$ values of n-alkanes from lake sediment from 18 cal ka BP, tropical NE Australia. Quat. Sci. Rev. 337, 108807.
Liu, J., An, Z., 2019. Variations in hydrogen isotopic fractionation in higher plants and sediments across different latitudes: Implications for paleohydrological reconstruction. Sci. Total Environ. 650, 470–478.
Mark, S.Z., Abbott, M.B., Rodbell, D.T., Moy, C.M., 2022. XRF analysis of Laguna Pallcacocha sediments yields new insights into Holocene El Niño development. Earth Planet. Sci. Lett. 593, 117657.
May, J.H., Preusser, F., Gliganic, L.A., 2015. Refining late Quaternary plunge pool chronologies in Australia's monsoonal 'top end. Quat. Geochronol. 30, 328–333.
McGowan, H., Marx, S., Moss, P., Hammond, A., 2012. Evidence of ENSO mega-drought triggered collapse of prehistory Aboriginal society in Northwest Australia. Geophys. Res. Lett. 39 (22).
McGregor, H.V., Fischer, M.J., Gagan, M.K., Fink, D., Phipps, S.J., Wong, H., Woodroffe, C.D., 2013. A weak El Niño/Southern Oscillation with delayed seasonal growth around 4,300 years ago. Nat. Geosci. 6 (11), 949.
McRobie, F.H., Stemler, T., Wyrwoll, K.H., 2015. Transient coupling relationships of the Holocene Australian monsoon. Quat. Sci. Rev. 121, 120–131.
Mohtadi, M., Oppo, D.W., Steinke, S., Stuut, J.B.W., De Pol-Holz, R., Hebbeln, D., Lückge, A., 2011. Glacial to Holocene swings of the Australian–Indonesian monsoon. Nat. Geosci. 4 (8), 540.
Moy, C.M., Seltzer, G.O., Rodbell, D.T., Anderson, D.M., 2002. Variability of El Niño/Southern Oscillation activity at millennial timescales during the Holocene epoch. Nature 420 (6912), 162–165.
Munksgaard, N.C., Wurster, C.M., Bird, M.I., 2011. Continuous analysis of δ18O and δD values of water by diffusion sampling cavity ring-down spectrometry: a novel sampling device for unattended field monitoring of precipitation, ground and surface waters. Rapid Commun. Mass Spectrom. 25 (24), 3706–3712.
Munksgaard, N.C., Kurita, N., Sánchez-Murillo, R., Ahmed, N., Araguas, L., Balachew, D. L., Bird, M.I., Chakraborty, S., Kien Chinh, N., Cobb, K.M., Ellis, S.A., 2019. Data Descriptor: Daily observations of stable isotope ratios of rainfall in the tropics. Sci. Rep. 9 (1), 14419.
Nott, J., Price, D., 1994. Plunge pools and paleoprecipitation. Geology 22 (11), 1047–1050.
Nott, J., Price, D., 1999. Waterfalls, floods and climate change: evidence from tropical Australia. Earth Planet. Sci. Lett. 171 (2), 267–276.
Parish, M., Russell, J., Konecky, B., Du, X., He, C., Bijaksana, S., Vogel, H., 2024. Changes in Indo-Pacific warm Pool hydroclimate and vegetation during the last deglaciation. Quat. Sci. Rev. 336, 108755.
Peel, M.C., Finlayson, B.L., McMahon, T.A., 2007. Updated world map of the Köppen-Geiger climate classification. Hydrol. Earth Syst. Sci. Discuss. 4 (2), 439–473.
Pope, M., Jakob, C., Reeder, M.J., 2009. Regimes of the north Australian wet season. J. Clim. 22 (24), 6699–6715.
Rowe, C., Brand, M., Hutley, L.B., Wurster, C., Zwart, C., Levchenko, V., Bird, M., 2019. Holocene savanna dynamics in the seasonal tropics of northern Australia. Rev. Palaeobot. Palynol. 267, 17–31.
Ruan, Y., Mohtadi, M., van der Kaars, S., Dupont, L.M., Hebbeln, D., Schefuß, E., 2019. Differential hydro-climatic evolution of East Javanese ecosystems over the past 22,000 years. Quat. Sci. Rev. 218, 49–60.
Sachse, D., Billault, I., Bowen, G.J., Chikaraishi, Y., Dawson, T.E., Feakins, S.J., Freeman, K.H., Magill, C.R., McInerney, F.A., Van Der Meer, M.T., Polissar, P., 2012. Molecular paleohydrology: interpreting the hydrogen-isotopic composition of lipid biomarkers from photosynthesizing organisms. Annu. Rev. Earth Planet. Sci. 40, 221–249.
Scott, R., 2001. Black Hawk down. Columbia Pictures, United States.
Scroxton, N., Gagan, M.K., Ayliffe, L.K., Hantoro, W.S., Hellstrom, J.C., Cheng, H., Edwards, R.L., Zhao, J.X., Suwargadi, B.W., Rifai, H., 2022. Antiphase response of the Indonesian–Australian monsoon to millennial-scale events of the last glacial period. Sci. Rep. 12 (1), 20214.
Shulmeister, J., Lees, B.G., 1995. Pollen evidence from tropical Australia for the onset of an ENSO-dominated climate at c. 4000 BP. The Holocene 5 (1), 10–18.
Steinke, S., Mohtadi, M., Prange, M., Varma, V., Pittauerova, D., Fischer, H.W., 2014a. Mid-to late-Holocene Australian–Indonesian summer monsoon variability. Quat. Sci. Rev. 93, 142–154.
Steinke, S., Mohtadi, M., Prange, M., Varma, V., Pittauerova, D., Fischer, H.W., 2014b. Mid-to late-Holocene Australian–Indonesian summer monsoon variability. Quat. Sci. Rev. 93, 142–154.
Sun, W., Zhang, E., Rowe, C., Bird, M.I., 2025. Holocene climate changes in tropical Australasia based on branched tetraether lipid evidence from Girraween Lagoon, northern Australia. Catena 256, 109124.
Suppiah, R., 1992. The Australian summer monsoon: a review. Prog. Phys. Geogr. 16 (3), 283–318.

Wang, P.X., Wang, B., Cheng, H., Fasullo, J., Guo, Z., Kiefer, T., Liu, Z., 2017. The global monsoon across time scales: Mechanisms and outstanding issues. Earth Sci. Rev. 174, 84–121.
Wasson, R., Bayliss, P., Clelland, S., 2007. River flow and climate in the 'top end'of Australia for the last 1000 years, and the Asian-Australian monsoon. In: Kakadu National Park Landscape Symposia Series, 2009, pp. 15–31.
Wheeler, M.C., McBride, J.L., 2005. Australian-INdonesian Monsoon. In: Lau, W.K.M., Waliser, D.E. (Eds.), Intraseasonal variability in the atmosphere-ocean climate system. Praxis Publishing, Chchester, UK, pp. 125–174.
White, S.M., Ravelo, A.C., Polissar, P.J., 2018. Dampened El Niño in the early and Mid-Holocene due to Insolation-Forced Warming/Deepening of the Thermocline. Geophys. Res. Lett. 45 (1), 316–326.
Woodroffe, C.D., Gagan, M.K., 2000. Coral microatolls from the Central Pacific record late Holocene El Nino. Geophys. Res. Lett. 27 (10), 1511–1514.
Wurster, C.M., Rowe, C., Zwart, C., Sachse, D., Levchenko, V., Bird, M.I., 2021. Indigenous impacts on north Australian savanna fire regimes over the Holocene. Scientific Reports 11 (1), 23157.
Wurtzel, J.B., Abram, N.J., Lewis, S.C., Bajo, P., Hellstrom, J.C., Troitzsch, U., Heslop, D., 2018. Tropical Indo-Pacific hydroclimate response to North Atlantic forcing during the last deglaciation as recorded by a speleothem from Sumatra, Indonesia. Earth Planet. Sci. Lett. 492, 264–278.
Wyrwoll, K.H., Miller, G.H., 2001. Initiation of the Australian summer monsoon 14,000 years ago. Quat. Int. 83, 119–128.
Wyrwoll, K.H., Liu, Z., Chen, G., Kutzbach, J.E., Liu, X., 2007. Sensitivity of the Australian summer monsoon to tilt and precession forcing. Quat. Sci. Rev. 26 (25–28), 3043–3057.
Wyrwoll, K.H., Hopwood, J.M., Chen, G., 2012. Orbital time-scale circulation controls of the Australian summer monsoon: a possible role for mid-latitude Southern Hemisphere forcing? Quat. Sci. Rev. 35, 23–28.
Xu, C., Wang, S.Y.S., Borhara, K., Buckley, B., Tan, N., Zhao, Y., An, W., Sano, M., Nakatsuka, T., Guo, Z., 2023. Asian-Australian summer monsoons linkage to ENSO strengthened by global warming. Npj climate and Atmospheric. Science 6 (1), 8.
Zhang, J., Liang, M.Q., Li, T.Y., Chen, C.J., Li, J.Y., 2022. Asian-Australian monsoon evolution over the last millennium linked to ENSO in composite stalagmite δ18O records. Quat. Sci. Rev. 281, 107420.
Zwart, C., Munksgaard, N.C., Protat, A., Kurita, N., Lambrinidis, D., Bird, M.I., 2018. The isotopic signature of monsoon conditions, cloud modes, and rainfall type. Hydrol. Process. 32 (15), 2296–2303.